Unsteady relaxation of a thin sheet in a quiescent fluid

Kirill Goncharuk, Saichand Chowkampally, Yuri Feldman, and Oz Oshri*
Department of Mechanical Engineering, Ben-Gurion University of the Negev, Beer-Sheva 84105, Israel

(Received 25 August 2025; accepted 18 February 2026; published 6 April 2026)

Slender elastic structures that interact with surrounding fluids are common in many biological and engineering settings. Motivated by these applications, we investigate the dynamics of a thin elastic sheet that is initially held in a laterally compressed configuration within a quiescent fluid, and then released from rest. As the sheet tries to recover its minimum energetic shape, its motion is governed by a subtle balance between elasticity, inertia, and fluid resistance. We begin by focusing on the early-time behavior and derive an analytical model in the inviscid limit, capable of predicting the oscillation frequency around the first buckling mode of the sheet and the growth rate near the unstable second mode. These predictions are in close agreement with numerical simulations of the more complex viscous formulation of the fluid, and show strong dependence on the sheet-to-fluid inertia ratio. At later times we analyze the sheet's transition from the second to the first buckling mode. We find that the inviscid model continues to track the system's evolution with good accuracy. In particular, we identify a logarithmic scaling for the transition time, which is also well supported by our numerical results. Altogether, our findings suggest that even in viscous environments, inviscid models can offer valuable insight into transient elastohydrodynamic processes.

DOI: 10.1103/ck8l-pv89

I. INTRODUCTION

In many natural and engineered systems, slender structures are immersed in fluid environments, where their motion and deformation are closely coupled to the surrounding flow [1–5]. From the undulating motion of aquatic vegetation stirred by a passing wave [6] to the controlled deployment of soft materials in microfluidic devices [7,8], the interaction between elastic bodies and viscous media leads to diverse and complex dynamic behaviors. Among these, a growing focus has been placed on systems where bent or buckled elastic structures are immersed in fluid and then released, initiating dynamic relaxation driven by fluid-structure interactions [9–12]. Such processes have practical applications in areas ranging from biomedical device actuation to energy harvesting in systems undergoing transient elastic deformations [13–16].

In this study, we focus on a simple yet dynamically rich scenario: a thin elastic sheet is initially held in a laterally compressed (bent) configuration and then released inside a quiescent fluid. The sudden release sets the sheet into motion, and its elastic relaxation generates flow in the surrounding medium. This unsteady motion couples inertia, elasticity, and fluid viscosity in a nontrivial way, and produces complex transient responses that are both theoretically challenging and practically relevant. Such problems arise, for instance, in the deployment of flexible films in soft robotics [17], the morphing of biological tissues [18], or the reconfiguration of flexible materials under hydrodynamic load [19].

We analyze the coupled dynamics of the elastic sheet and the surrounding fluid with the aim of understanding the mechanisms that govern the relaxation process. The study focuses on character-

*Contact author: oshrioz@bgu.ac.il

izing the flow fields induced by the sheet's motion and identifying scaling laws that describe the evolution of the system. At early times, and at relatively high Reynolds numbers, the dynamics are shown to be well approximated by treating the surrounding fluid as inviscid. To capture this transient motion, we develop an analytical framework that combines the mechanics of thin elastic sheets with the hydrodynamics of inviscid fluids. In the limit of small deflections, the model simplifies considerably, and weakly nonlinear approximations provide an accurate description of the system's evolution.

Focusing on the dynamics at early times, we derive explicit expressions for the frequency of oscillations around the sheet's first mode of buckling, as well as the growth rate of the system when the sheet initially accommodates the (unstable) second mode. Here, the first buckling mode refers to the lowest-order buckling configuration, while the second mode corresponds to the next higher-order configuration with an additional half-wavelength. These analytical predictions are found to be in good agreement with numerical simulations that incorporate the nonlinear elastohydrodynamic formulation, which includes, *inter alia*, viscosity and higher-order nonlinearities of the elastic model [9]. We find that both the frequency and the growth rate depend strongly on the sheet-to-fluid inertia ratio, λ, where length and time are normalized by the total length of the sheet and its inertial timescale, respectively.

Just beyond the initial stages, we examine the system's evolution as the sheet transitions from the second mode to the first buckling mode. Despite the increasing complexity of the flow and deformation fields at later times, we find that the inviscid formulation continues to capture the dynamics with surprising accuracy. In particular, we analyze the time it takes for the sheet to release its stored bending energy and reach the first buckling mode. We show that this transition time scales as $\sigma t_{\mathrm{p}} \sim \ln(\Delta^{1/2}/h_0)$, where t_{p} denotes the duration of the second-to-first mode transition, σ is the growth rate, Δ is the lateral displacement of the sheet, and h_0 represents the initial deviation from the second mode. This scaling shows very good agreement with results from the viscous formulation.

The paper is organized as follows. In Sec. II, we formulate the problem, introduce the variational approach, and present the modal expansion of the elastic and hydrodynamic fields. Section III is devoted to the linear stability analysis of the system: we first derive the governing equations and then use them to obtain expressions for the oscillation frequency around the first buckling mode and the growth rate associated with the second, unstable mode. In Sec. IV, we examine the dynamics at later times and derive the scaling law for the transition time t_{p}. Finally, in Sec. V, we summarize the main results and suggest directions for future studies.

II. FORMULATION OF THE PROBLEM

An inextensible thin sheet of length L, thickness h, bending modulus B, and density ρ_{sh} is placed in an infinite, inviscid fluid of density ρ_{f}. The two ends of the sheet are hinged and are separated by a distance $L - \Delta$ along the x axis; see Fig. 1 for a schematic illustration. At time $t < 0$, the sheet is at rest and, through the application of external forces, adopts an arbitrary configuration that satisfies the constraints of inextensibility and end-to-end shortening. At $t \geqslant 0$, these forces are removed, and the sheet freely evolves within the fluid. The system is assumed two-dimensional, such that the dynamics is confined to the xy plane. Hereafter, we normalize all lengths to the total length of the sheet L and time to the inertial timescale of the sheet $L^2\sqrt{\rho_{\mathrm{sh}}h/B}$.

Within the small-amplitude approximation, the configuration of the sheet is described by the height function $y_{\mathrm{sh}}(x, t)$, where $x \in [0, 1]$ is the dimensionless coordinate along the undeformed sheet axis, and by the axial force per unit length $F_x(t)$ that enforces the end-to-end constraint. Here, $F_x(t)$ is normalized by B/L^2. Additionally, the state of an irrotational and inviscid fluid is determined by the potential function $\phi(x, y, t)$, from which we can calculate the fluid velocity by $\mathbf{v}(x, y, t) = \nabla\phi$, where ∇ is the two-dimensional gradient operator. For completeness, Appendix A presents the reduction of the nonlinear elastic model coupled to the viscous Navier–Stokes equations to the inviscid formulation.

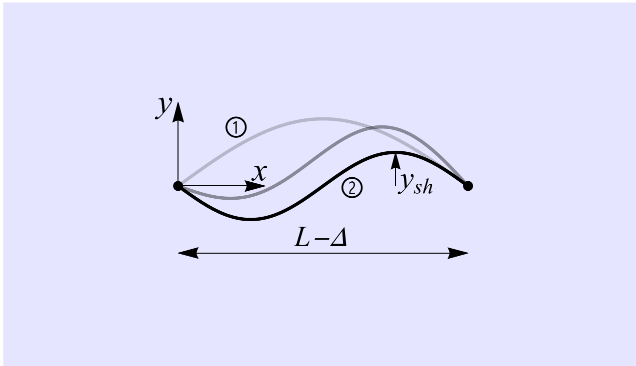

FIG. 1. Schematic overview of the system. A thin sheet is immersed in a fluid medium and subjected to lateral compression. The sheet is released from rest in a configuration with higher bending energy than its minimum-energy state. The circled labels indicate the first ① and second ② buckling modes of the sheet, that correspond, respectively, to the stable single-half-wavelength configuration and the unstable higher-order configuration with an additional half-wavelength. The subsequent analysis focuses on small oscillations about the first (stable) buckling mode and on the relaxation dynamics from the second (unstable) buckling mode toward the first.

In previous publications [10,11,20], we demonstrated that the dynamics of such systems are governed by the minimization of the action $\mathcal{S} = \int_0^T \mathcal{L}\, dt$, where T denotes the time of the evolution and $\mathcal{L}$ is a Lagrangian given by

$$\mathcal{L} = \int_0^1 \left[\frac{1}{2}\left(\frac{\partial y_{\rm sh}}{\partial t}\right)^2 - \frac{1}{2}\left(\frac{\partial^2 y_{\rm sh}}{\partial x^2}\right)^2 + F_x(t)\left(\frac{1}{2}\left(\frac{\partial y_{\rm sh}}{\partial x}\right)^2 - \Delta\right) + \frac{1}{\lambda}[\phi(x,0^-,t) - \phi(x,0^+,t)]\frac{\partial y_{\rm sh}}{\partial t}\right] dx - \frac{1}{2\lambda}\int_{-\infty}^{\infty}\int_{-\infty}^{\infty} |\nabla\phi|^2 dx dy, \tag{1}$$

where $\phi(x, 0^+, t)$ ($\phi(x, 0^-, t)$) denotes the limit $y \to 0$ from above (below), and we require that the fluid remains at rest at infinity. In addition, the area integral in the second line of Eq. (1) is taken over the entire xy plane, excluding the line occupied by the sheet. The terms appearing in the Lagrangian have clear physical interpretations. The first and second terms account for the small-amplitude kinetic and bending energies of the sheet. In particular, in the small-slope limit, the curvature-squared contribution to the bending energy reduces to the square of the second derivative of the height function. The third term enforces the inextensibility constraint, with $F_x(t)$ acting as a Lagrange multiplier that fixes the end-to-end shortening of the sheet. The fourth term represents the coupling between the sheet and the surrounding fluid, and contributes both to the pressure exerted by the fluid on the sheet and to the kinematic boundary condition. Finally, the last term in Eq. (1) corresponds to the kinetic energy of the fluid.

In addition, we further define the parameter $\lambda = \rho_{\rm sh} h/(\rho_{\rm f} L)$, which measures the ratio of sheet inertia to fluid inertia. In the present incompressible and irrotational setting, the characteristic vertical extent of the fluid motion is set by the sheet length L. This follows from the fact that the hydrodynamic potential satisfies Laplace's equation, which enforces comparable length scales in the horizontal and vertical directions. As a result, the effective fluid inertia involved in the motion scales with the sheet length in the same manner as the horizontal deformation, leading naturally to the definition of the inertia ratio. This situation differs from the compressible case [10], where the fluid dynamics are governed by a wave equation, and the vertical wave number generally differs from that in the horizontal direction.

To make further analytical progress, we expand the function $y_{\mathrm{sh}}(x, t)$ in a Fourier series that satisfies the hinged boundary conditions at the sheet's edges:

$$y_{\mathrm{sh}}(x, t) = \sum_{n=1}^{N} A_n(t) \sin(\pi n x), \tag{2}$$

where $A_n(t)$ are as yet unknown time-dependent amplitudes. As we shall see later in the analysis, these sine functions correspond to the buckling modes of an inextensible, laterally compressed sheet with hinged boundary conditions. This choice, therefore, provides a natural basis for describing both the buckled configurations and the subsequent dynamics. In addition, the solution for the fluid's potential function is expressed in terms of a vortex distribution along the sheet's contour [21]:

$$\phi(x, y, t) = -\frac{1}{2\pi} \int_0^1 \gamma(x_0, t) \tan^{-1}\left(\frac{y}{x - x_0}\right) dx_0, \tag{3}$$

where $\gamma(x_0, t)$ is the strength of the vorticity per unit length at time t.

Now, consider a closed loop surrounding the sheet. Since the system is initially at rest, the circulation along this loop is zero at $t = 0$ and, according to Kelvin's circulation theorem, must remain zero at all later times [22]. Because circulation is proportional to the total vorticity enclosed within the loop, the vorticity must also remain zero throughout the motion. These considerations motivate the following Fourier expansion for the vorticity distribution:

$$\gamma(x, t) = \sum_{n=1}^{N} a_n(t) \cos(\pi n x). \tag{4}$$

Equations (2)–(4) imply the explicit dependence of the sheet and the fluid on the spatial coordinates. As such, we can substitute these expansions into the Lagrangian equation (1) and perform the integration. Additionally, we can readily minimize the Lagrangian with respect to $a_n(t)$ and express these amplitudes as functions of $A_n(t)$. Further details of this analysis are given in Appendix C. Overall, this procedure gives

$$\mathcal{L} = T_{nk} \frac{dA_n}{dt} \frac{dA_k}{dt} - V_{nk} A_n A_k + F_x(t) C_{nk} A_n A_k - F_x(t) \Delta, \tag{5}$$

where the Einstein summation rule for repeated indices is implied, and we define the following matrices:

$$T_{nk} = \frac{1}{4}\delta_{nk} + \frac{1}{4\pi^2 \lambda n k}\left(D_{sr}\tilde{D}^{-1}_{rn}\tilde{D}^{-1}_{sk} - \tilde{D}^{-1}_{nk}\right), \quad V_{nk} = \frac{\pi^4 n^4}{4}\delta_{nk}, \quad C_{nk} = \frac{\pi^2 n^2}{4}\delta_{nk}, \tag{6a}$$

$$D_{nk} = -\frac{1}{4\pi^2 k} \int_0^1 \sin(\pi k x)\left(\mathrm{P.V} \int_0^1 \frac{\cos(\pi n x_0)}{x - x_0} dx_0\right) dx, \quad \tilde{D}_{nk} = D_{nk} + D_{kn}, \tag{6b}$$

where P.V in Eq. (6b) corresponds to a principal value integral [23]. The minimization of the Lagrangian (5) yields the following equations of motion:

$$T_{nk} \frac{d^2 A_k}{dt^2} + (V_{nk} - F_x(t) C_{nk}) A_k = 0 \tag{7a}$$

$$C_{nk} A_n A_k = \Delta. \tag{7b}$$

Equation (7) represents a major simplification of the problem. Instead of tackling a complex set of partial differential equations, with rather involved boundary conditions, we are left to determine the time evolution of the modal amplitudes $A_n(t)$. This direction becomes particularly simple when only a few modes participate in the motion, as in the cases we further consider in the next sections.

III. LINEAR STABILITY

Our formulation allows for a straightforward examination of the sheet's stability around static equilibrium states. Among these equilibrium states, the first and second modes of buckling are of particular interest, since they are relatively easy to achieve experimentally. A laterally confined sheet naturally adopts the first mode of buckling because it corresponds to its minimum energy state. As a result, any deviation from this state leads to periodic oscillations, whose frequency can be determined by the linear stability analysis. The second buckling mode can be induced, for example, by constraining the sheet's height to zero at its midpoint while applying lateral compression. However, once the midpoint constraint is removed, the second buckling mode becomes unstable, and linear stability analysis can then be used to determine the growth rate of the fastest-growing mode. These frequencies and growth rates have been evaluated either for thin sheets in the absence of a surrounding fluid, or for sheets immersed in fluid confined within a box or channel [20,24]. With our approach, we can first predict the effect of an unconstrained fluid on these values.

To derive the linear stability equations, we expand the modal amplitudes and the axial force around their base solutions: $A_n(t) = A_n(0) + \epsilon e^{\sigma t}\tilde{A}_n$ and $F_x(t) = F_x(0) + \epsilon e^{\sigma t}\tilde{F}_x$, where $A_n(0)$ and $F_x(0)$ are the equilibrium solutions, $\epsilon \ll 1$ is a small parameter, σ is the growth rate, and $\tilde{A}_n$ and $\tilde{F}_x$ are unknown coefficients. By substituting these expansions into Eq. (7), we obtain at order ϵ^0

$$(V_{nk} - F_x(0)C_{nk})A_k(0) = 0, \tag{8a}$$

$$C_{nk}A_n(0)A_k(0) = \Delta, \tag{8b}$$

and at the linear order we have

$$[\sigma^2 T_{nk} + V_{nk} - F_x(0)C_{nk}]\tilde{A}_k - C_{nk}A_k(0)\tilde{F}_x = 0, \tag{9a}$$

$$C_{nk}A_n(0)\tilde{A}_k = 0. \tag{9b}$$

To obtain the growth rate, we first need to solve Eq. (8) to determine the equilibrium state. Then, by substituting this zeroth-order solution into Eq. (9), we obtain a set of linear and homogeneous equations that have a nontrivial solution when their corresponding determinant vanishes. This condition yields the parameter σ.

It is straightforward to show that the zeroth-order solutions of the first ($n = 1$) and the second ($n = 2$) buckling modes are given by

$$A_n(0) = \frac{2\sqrt{\Delta}}{\pi n}, \quad F_x(0) = (\pi n)^2, \tag{10}$$

where $A_k(0) = 0$ for all $k \neq n$. With these solutions, it is only left to determine σ from Eq. (9). This is considered in the following sections.

A. Linear stability around the first mode

As we now show, adopting the two-mode approximation, wherein $N = 2$, already yields a very good approximation to the solution. We compare our results with numerical simulations of the Navier-Stokes equations coupled to the nonlinear description of a thin sheet. Details of these equations are given in Appendix A.

To obtain the frequency of vibrations around the first mode of buckling, we substitute Eq. (10) with $n = 1$ in Eq. (9). This gives $\tilde{A}_1 = \tilde{F}_x = 0$, i.e., while the base solution is described by an even shape of the sheet, it is primarily perturbed by $\tilde{A}_2$ that corresponds to an odd configuration. Indeed, a nontrivial solution is obtained when $\tilde{A}_2$ remains arbitrary, and the growth rate takes an imaginary value $\sigma = i\omega$, where

$$\omega = \frac{2\sqrt{3}\pi^2}{\sqrt{1 + \frac{|\tilde{D}_{22}^{-1}|}{8\pi^2\lambda}}}, \tag{11}$$

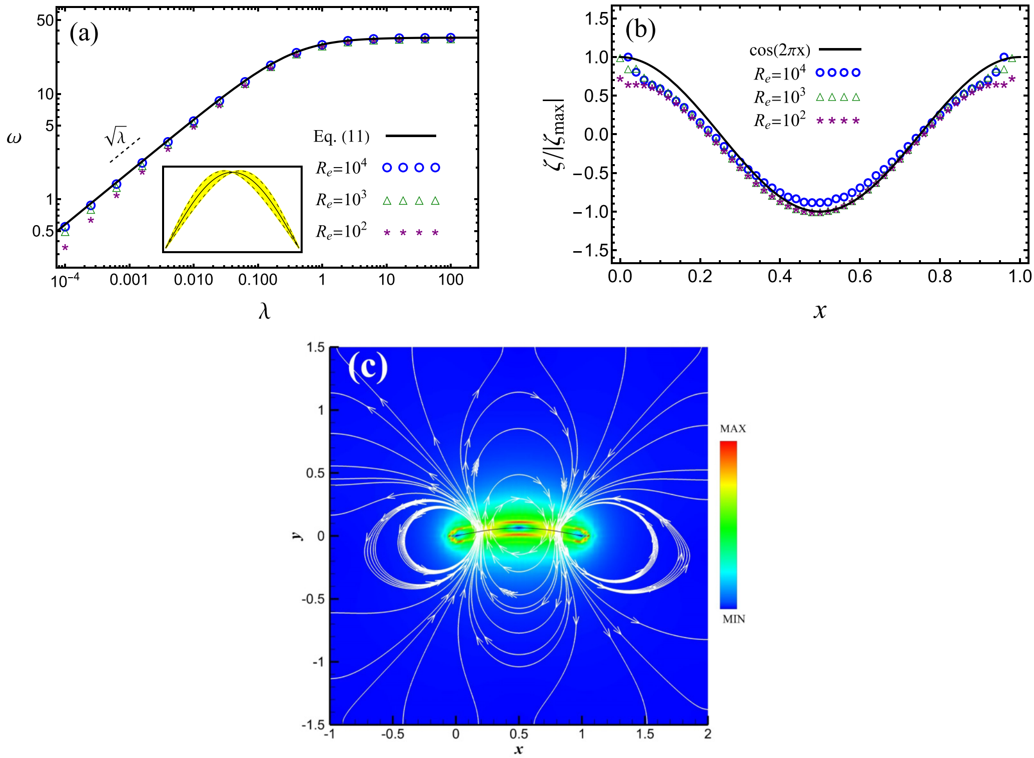

FIG. 2. Linear stability analysis around the first mode of buckling. (a) The frequency ω as a function of the sheet-to-fluid inertia ratio λ. Symbols correspond to the linear stability problem at different Reynolds numbers, and the solid line to the analytical prediction, Eq. (11). The inset presents a schematic illustration of the sheet's vibrations. Solid line corresponds to the base solution, i.e., the first mode of buckling, and the dashed lines correspond to a superposition of the base solution and the perturbation. (b) The vorticity eigenfunction along the contour of the sheet, normalized to the point on the sheet with maximum vorticity, obtained from the linear stability analysis of the viscous formulation ($\lambda = 0.1$) in comparison with the analytical prediction. (c) The corresponding velocity eigenmode resulting from the sheet's oscillations, where $R_e = 10^3$ and $\lambda = 0.1$. Arrows represent the streamlines, and colors represent the relative magnitudes of the velocity. The numerical data in all panels is presented for $\Delta = 0.01$.

and $|\tilde{D}_{22}^{-1}| \simeq 27.83$. In Fig. 2(a), we plot the frequency of vibrations as a function of λ and compare the results with the linear stability analysis of the viscous formulation. While our inviscid model yields a purely imaginary growth rate, as it does not account for fluid dissipation, the viscous formulation produces a growth rate with a nonzero real part. The comparison in Fig. 2(a) considers only the imaginary part of the numerical solution. Overall, the analytical and viscous solutions agree well at high Reynolds numbers $R_e \sim 10^3$, where $R_e = (\rho_f/\mu)\sqrt{B/\rho_{sh}h}$ and μ is the fluid viscosity, but significant deviations appear when $R_e \sim 10^2$. The inset in Fig. 2(a) illustrates the sheet's oscillations around the base solution. When the first mode (solid line) is perturbed by the second mode, the sheet appears to move from left to right while its midpoint remains stationary.

When the sheet's inertia dominates the fluid's inertia ($\lambda \gg 1$), the frequency converges to a λ-independent constant, $\omega \simeq 2\sqrt{3}\pi^2$, as expected in the absence of a confining fluid [20]. This saturation reflects the oscillation timescale set solely by the sheet inertia, but is not typically realized in experiments, since reaching this limit generally requires shorter or thicker sheets than are commonly used. For realistic material and fluid parameters, the crossover toward this plateau occurs at $\lambda \sim 10$, so most experimental systems are expected to lie in an intermediate regime where both sheet and fluid inertia contribute. In this context, it is important to note that in the inextensible, hinged setting considered here, the axial force in the base state is independent of the end-shortening Δ, and as a result, the oscillation frequency is also independent of Δ. In contrast, models with finite extensibility exhibit a Δ-dependent frequency that vanishes near the onset [24].

However, for smaller values of λ, the presence of the fluid may significantly reduce the frequency. In fact, in the opposite limit of $\lambda \ll 1$, the frequency scales as $\omega \propto \sqrt{\lambda}$. These two asymptotic regions can be understood as follows. When $\lambda \gg 1$, the hydrodynamic pressure exerted by the fluid on the sheet becomes negligible, and the forces of bending and lateral compression are balanced solely by the sheet's inertia. In contrast, when $\lambda \ll 1$, the overall dynamics slow down due to the fluid's resistance to motion, and the internal forces of bending and compression are balanced entirely by the hydrodynamic pressure. This leads to the observed λ-dependent frequency.

Given that $\tilde{A}_1 = 0$, Eqs. (4) and (C3) imply that, in the two-mode approximation, the vortex distribution on the sheet is proportional to $\gamma(x,t) \propto \cos(2\pi x)$. This prediction can indeed be verified numerically by calculating the vorticity field $\zeta = \frac{\partial v_y}{\partial x} - \frac{\partial v_x}{\partial y}$ very close to the contour of the sheet, where v_x and v_y are the fluid velocities in the x and y directions, respectively. The resulting vorticity profile qualitatively resembles the analytical prediction; see Fig. 2(b). It should be emphasized that, unlike in the analytical solution, where vorticity stems from point sources located exactly on the contour of the sheet and not in the fluid, in the numerical solution, the vorticity arises from actual velocity gradients, which typically form within boundary layers around the region of the sheet.

The vorticity reaches extremal values at the two ends of the sheet and at its midpoint, with the vorticity at the ends having the opposite sign to that at the midpoint. This distribution generates the flow field shown in Fig. 2(c), where each end of the sheet forms the center of a vortex rotating in the same direction, while the midpoint forms the center of another vortex rotating in the opposite direction. The magnitude of the fluid velocity diminishes to zero away from the sheet.

B. Linear stability around the second mode

Let us now adopt the two-mode approximation to estimate the growth rate of the system when the sheet initially accommodates the second buckling mode. Substituting the base solution [Eq. (10) with $n = 2$] into Eq. (9), we find that $\tilde{A}_2 = \tilde{F}_x = 0$; that is, while the base solution has an asymmetric shape, it is primarily perturbed by the first mode, which is symmetric. Indeed, we find a nontrivial solution when $\tilde{A}_1$ remains arbitrary, and the growth rate is given by

$$\sigma = \frac{\sqrt{3}\pi^2}{\sqrt{1 + \frac{|\tilde{D}_{11}^{-1}|}{2\pi^2\lambda}}}, \tag{12}$$

where $\tilde{D}_{11}^{-1} \simeq -16.24$. As expected, the growth rate of the fastest-growing mode is always positive, and so the sheet tends to escape from the second mode for all values of λ. This analytical prediction is compared with the numerical solution in Fig. 3(a) for three different values of R_e. While at high Reynolds numbers, the numerical solution agrees well with Eq. (12), significant deviations appear at lower values, $R_e = 10^2$. As in the case of the first mode, the solution for σ converges to a λ-independent value when the sheet inertia dominates the fluid inertia, and exhibits square-root dependence in the opposite limit of $\lambda \ll 1$.

Following Eqs. (4) and (C3), we find that the vortex distribution on the sheet is proportional to $\gamma(x,t) \propto \cos(\pi x)$, in reasonable agreement with the numerical solution; see the comparison in Fig. 3(b). The differences between the two solutions may stem from higher modes that are neglected in the approximated solution. This distribution gives rise to two counter-rotating vortices located near the ends of the sheet; see Fig. 3(c). At the center, the vortices induce a local net flow, as their streamlines are oriented in the same direction.

As the sheet escapes from the second buckling mode, its elastic energy is gradually converted into kinetic energy of both the sheet and the surrounding fluid. This conversion drives the sheet toward

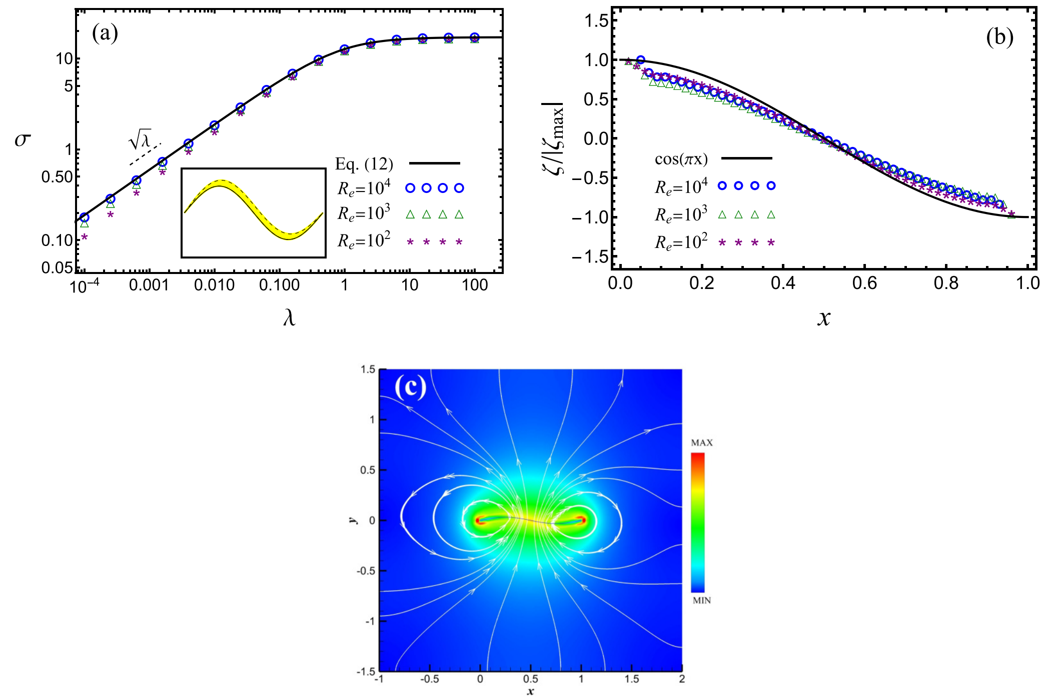

FIG. 3. Growth rate and flow field around the second buckling mode. (a) Growth rate σ as a function of the sheet-to-fluid inertia ratio λ. The solid line represents the analytical prediction [Eq. (12)], and the symbols correspond to the numerical solution of the linear stability problem for the viscous formulation. The inset schematically illustrates the escape of the sheet from the base solution: the solid line corresponds to the second mode, and the dashed line to a superposition of the second and first modes. (b) The vorticity eigenmode along the contour of the sheet, normalized by its maximum value, obtained from the linear stability analysis for $\lambda = 0.1$. Symbols represent numerical data, and the solid line shows the fitted function. (c) The corresponding velocity eigenmode in the fluid obtained from the linear stability analysis of the viscous formulation, shown for $R_e = 1000$ and $\lambda = 0.1$. Arrows indicate streamlines, and color represents the relative magnitude of the flow velocity. The numerical data in all panels is presented for $\Delta = 0.01$.

the configuration of lowest potential energy, i.e., the first buckling mode. Near this configuration, a portion of the kinetic energy is converted back into bending energy, causing the sheet to reverse direction. This back-and-forth behavior results in oscillations between kinetic and bending energies, which are progressively damped by fluid resistance until the system settles into the first-mode configuration. While this entire dynamics lies beyond the scope of our inviscid formulation, our model does capture the first transition from the second to the first mode. However, since this process occurs over longer timescales, beyond the reach of linear stability analysis, we must extend our approach to the weakly nonlinear regime. We refer to this stage of the dynamics as "moderate times" and analyze it in the next section.

Before turning to the next section, we note that a similar instability mechanism arises when the sheet is initialized in higher buckling modes. We return to this point in Appendix D, where stability and relaxation from the third buckling mode are analyzed within the same formalism.

IV. EVOLUTION AT MODERATE TIMES

Since the fluid in our model is inviscid and the deformation of the sheet is considered elastic, the total energy in the system is conserved. To obtain this energy from the small-amplitude

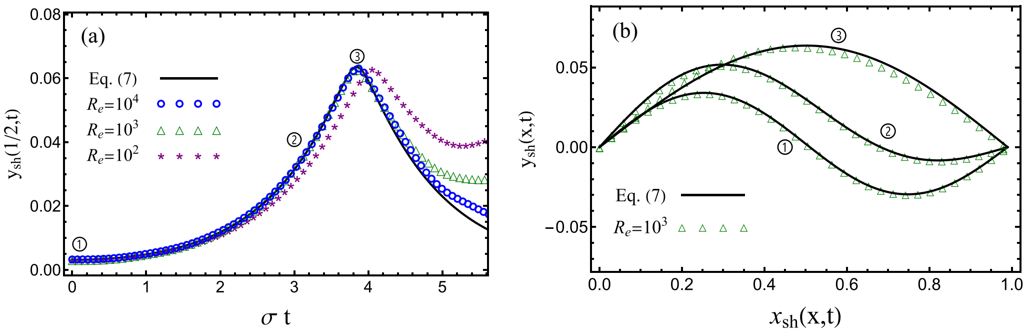

FIG. 4. The sheet's evolution at moderate times. In both panels, symbols represent numerical data and solid lines correspond to the solution of Eq. (7) with $N = 2$. We use $\lambda = 0.1$, $\Delta = 0.01$, and $h_0 = 0.0031$. (a) The sheet's midpoint as a function of time for three different values of the Reynolds number. Numbered labels correspond to times $\sigma t = 0.1, 3, 3.85$, where σ is given by Eq. (12). (b) The sheet's configurations at the times indicated in panel (a). Numerical data is shown for $R_e = 10^3$.

approximation, we first multiply Eq. (7a) by dA_n/dt and integrate over time. Then, we use the constraint given by Eq. (7b) to obtain $E = T_{nk}\frac{dA_n}{dt}\frac{dA_k}{dt} + V_{nk}A_nA_k$. The first term in the energy corresponds to the kinetic energies of the sheet and the fluid, while the second term corresponds to the potential energy of the sheet. This conservation of energy is the starting point of the following discussion.

Suppose that the sheet starts from rest in the unstable second mode, with a small perturbation added to this state. How long does it take for the sheet to first release its stored potential energy and reach the first buckling mode? The typical numerical evolution of this process is shown in Fig. 4 for three different Reynolds numbers. Panel (a) presents the evolution of the sheet's midpoint, and panel (b) shows three different configurations along the sheet's trajectory, indicated by corresponding labels in both panels. Initially, the midpoint height increases monotonically until reaching a peak displacement corresponding to a shape close to the first mode. After this point, the sheet reverses direction due to partial reconversion of kinetic energy into bending energy.

For comparison, we also plot in Fig. 4 the evolution predicted by the two-mode approximation, i.e., Eq. (7) with $N = 2$. The two solutions, numerical and analytical, agree well for the highest Reynolds number values up to the first peak, but show significant deviations beyond that point. This agreement between the two-mode approximation and the numerical solution at moderate times persists across different values of the system's parameters, and thus motivates the following analysis. This agreement likely stems from the fact that, in the early-time evolution, only two modes are significantly excited: the base state is dominated by the second mode, while the leading-order perturbation, according to the linear stability analysis, is governed by the first mode.

Since the system's dynamics are governed by only two modes, which are related through the inextensibility constraint [Eq. (7b)], the entire moderate-time dynamics can be reduced to a single first-order equation for one of the modes. To do that, we first eliminate, say, $A_2(t)$ in favor of $A_1(t)$ using Eq. (7b). Then, we obtain the energy as a function of $A_1(t)$ and its derivative alone. This gives the equation

$$\frac{dA_1}{dt} = \pm\sqrt{\frac{96\pi^8\lambda\left(\frac{4E}{3\pi^4} - \frac{16\Delta}{3\pi^2} + A_1^2\right)\left(\frac{4\Delta}{\pi^2} - A_1^2\right)}{24\pi^4\lambda\left(\frac{16\Delta}{3\pi^2} - A_1^2\right) + 64\Delta|\tilde{D}_{11}^{-1}| - \pi^2 c_1 A_1^2}}, \tag{13}$$

where $c_1 = 16|\tilde{D}_{11}^{-1}| - |\tilde{D}_{22}^{-1}| \simeq 232.0$ and $|\tilde{D}_{11}^{-1}| \simeq 16.24$ are numerical constants. When $A_1(t) = 0$, and the energy matches the elastic energy of the second mode ($E = 4\pi^2\Delta$), the right-hand side vanishes, and the system remains indefinitely in the unstable second mode. But if the initial state is only slightly perturbed from this mode, the system does not stay at rest and tends to escape from it.

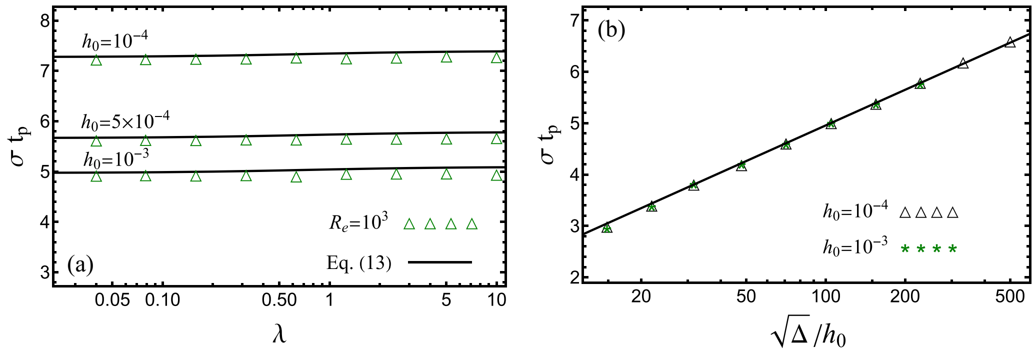

FIG. 5. The peak time as a function of the system parameters. In both panels logarithmic scale is used in the x axis. (a) σt_p as a function of λ. Symbols correspond to numerical simulations and solid line to the solution of Eq. (13), where $\Delta = 0.01$. (b) σt_p as a function of $\sqrt{\Delta}/h_0$. Solid line corresponds to Eq. (14) with $c \simeq 1.42$, and symbols represent the numerical data with $\lambda = 1$, $R_e = 10^3$, and $\Delta \in [10^{-6}, 10^{-2}]$.

We consider the initial condition $A_1(0) = h_0$ and $A_2(0) = \frac{1}{2}\sqrt{\frac{4\Delta}{\pi^2} - h_0^2}$, such that the system starts from rest with total energy $E = 4\pi^2\Delta - \frac{3\pi^4 h_0^2}{4}$, which is slightly below the energy of the second mode because the perturbation acts to release bending energy. In the limit $h_0 \ll 1$, we ask at what time t_p the sheet first reaches $A_1(t_\text{p}) = \frac{2\sqrt{\Delta}}{\pi}$, that corresponds to the first buckling mode; see Eq. (10) with $n = 1$. Of course, as h_0 decreases, the system is expected to escape more slowly from the unstable state. Our main interest lies in how the time t_p scales with the parameters λ, Δ, and h_0.

Since the system exhibits exponential growth at early times, we choose to measure time in units of $1/\sigma$, and focus on how σt_p, rather than t_p itself, depends on the system parameters. To obtain t_p, we integrate Eq. (13) numerically from h_0 to $2\sqrt{\Delta}/\pi$. The results, plotted in Fig. 5(a), demonstrate that the modified peak time σt_p is, to a good approximation, independent of the sheet-to-fluid inertia ratio λ. This implies that when $\lambda \gg 1$, the peak time converges to a constant independent of λ, whereas for $\lambda \ll 1$, we find $t_\text{p} \propto \lambda^{-1/2}$. Using this result, we can further examine the limit $h_0 \ll 1$ by eliminating λ in favor of σ via Eq. (12), and then substituting $\sigma = \sqrt{3}\pi^2$. Taking the limit $h_0 \to 0$, we obtain

$$\sigma t_\text{p} \simeq \ln\left(c\frac{\sqrt{\Delta}}{h_0}\right). \tag{14}$$

This relation is plotted in Fig. 5(b) and is shown to agree very well with the numerical data, where the proportionality constant is $c \simeq 1.42$.

While the analysis above focuses on relaxation from the second to the first buckling mode, the formulation is not restricted to this setting. In Appendix D, we extend the framework to the case where the sheet is initially prepared in the third buckling mode. We show that the linear stability problem excites lower modes and that the subsequent relaxation proceeds toward the lower modes. Notably, the logarithmic scaling of the transition time identified here persists for relaxations involving higher buckling modes, as discussed further in the Appendix.

V. SUMMARY AND CONCLUSIONS

In this work, we study the unsteady relaxation of a compressed sheet in a quiescent fluid. We showed that our model captures essential features of the transient coupling between the elastic sheet and the surrounding fluid. Its tractability and physical accuracy make it applicable to a broad class of systems, including biological tissues interacting with fluids, soft robotic components, and flexible structures operating in viscous environments. A central result of this study is an analytical description based on inviscid fluid dynamics, which successfully reproduces the system's behavior at both early and intermediate timescales. Within this framework, we derived scaling laws and closed-form expressions that closely match nonlinear simulations accounting for viscosity and geometric nonlinearities.

We derived explicit expressions for the frequency of oscillations around the first mode and for the growth rate associated with the second mode, both of which exhibit strong dependence on the sheet-to-fluid inertia ratio λ. These expressions converge to constant values when $\lambda \gg 1$, and follow a square-root scaling when $\lambda \ll 1$, with good agreement across the full range of λ when compared to numerical simulations. At later times, we examined the transition of the system from the second mode toward the first, and found that the inviscid model continues to predict the dynamics with surprising accuracy. In particular, we identified a logarithmic scaling for the transition time, $\sigma t_{\mathrm{p}} \sim \ln(\sqrt{\Delta}/h_0)$, which matches well with the results from the viscous formulation and captures the key dependence on the initial amplitude and lateral compression.

The dependence of the characteristic frequency and growth rate on the inertia ratio λ can be understood in terms of a crossover between two inertial regimes. For deformations with wavelength $O(L)$, the elastic restoring force associated with bending scales as BA/L^3, where A is the typical amplitude. In the limit $\lambda \ll 1$, the dominant inertial contribution comes from the surrounding fluid. For an incompressible and irrotational flow, the fluid set into motion extends over a vertical distance $O(L)$, so that the effective fluid inertia per unit width scales as $\rho_{\mathrm{f}} L^2$. The corresponding inertial force then scales as $\rho_{\mathrm{f}} L^2 \omega^2 A$. Balancing the elastic restoring force with the fluid inertial force then gives $\omega^2 \sim B/(\rho_{\mathrm{f}} L^5)$. When nondimensionalized using the sheet inertial timescale $\sqrt{B/(\rho_{\mathrm{sh}} h L^4)}$, this yields the square-root scaling $\omega \sim \sqrt{\lambda}$. In contrast, in the opposite limit $\lambda \gg 1$, the inertia of the sheet dominates, with an effective inertia per unit width scaling as $\rho_{\mathrm{sh}} hL$. The corresponding sheet inertial force scales as $\rho_{\mathrm{sh}} hL\omega^2 A$. In this case, balancing bending forces with sheet inertia leads directly to $\omega^2 \sim B/(\rho_{\mathrm{sh}} hL^4)$, so that the dimensionless frequency and growth rate approach λ-independent constants. This change in the dominant inertial contribution explains both the $\sqrt{\lambda}$ scaling at small λ and the plateau observed at large λ.

Moreover, the logarithmic dependence at moderate times follows from the exponential growth of the unstable mode in the early stage of the transition. If the relevant modal amplitude grows as $A(t) \simeq h_0 e^{\sigma t}$, then the time to reach an $O(\sqrt{\Delta})$ amplitude satisfies $\sqrt{\Delta} \sim h_0 e^{\sigma t_p}$, which yields $\sigma t_p \sim \ln(\sqrt{\Delta}/h_0)$.

Several directions for future investigation naturally emerge from this study. First and foremost, a more detailed understanding of viscous effects is needed to complement the inviscid framework developed here. For instance, numerical results from the linear stability analysis indicate that the eigenvalue associated with oscillations around the first buckling mode acquires a nonzero real part that corresponds to the hydrodynamic damping. The scaling of this real part with the Reynolds number and the sheet-to-fluid inertia ratio remains an open question. Moreover, in a viscous fluid, the oscillations of the sheet eventually decay, and the mechanism by which elastohydrodynamic interaction dissipates kinetic energy over successive cycles is not yet fully understood. In particular, at sufficiently large viscosities, one may expect a transition from underdamped to overdamped relaxation [25], a regime that is not captured by the inviscid formulation considered here. Beyond single-sheet dynamics, another compelling direction involves extending the analysis to multiple interacting sheets. One may ask, for example, whether a periodic array of sheets initialized in the second buckling mode behaves collectively, and whether hydrodynamic coupling between neighboring sheets slows down or modifies the relaxation dynamics relative to an isolated sheet.

More broadly, the results presented here provide a consistent framework for understanding the relaxation of buckled elastic beams immersed in viscous fluids. Although the present study is restricted to a confined geometry with discrete buckling modes, the observed transfer of energy toward lower modes bears a conceptual connection to relaxation processes reported for spatially extended sheets [26–28]. Exploring possible links between these discrete modal dynamics and continuum coarsening scenarios, therefore, remains an interesting direction for future work.

Altogether, our study reveals the rich transient dynamics governed by nonlinear geometry and coupled fluid-structure interactions. By combining analytical and numerical tools from thin-sheet elasticity and fluid dynamics, we identified key mechanisms that shape the transient response of elastic structures in fluid environments. The framework developed here lays the groundwork for exploring more complex elastohydrodynamic systems, where geometry, collective interactions, and dissipative effects play a significant role.

ACKNOWLEDGMENT

This research was partially supported by the Israel Science Foundation (Grant No. 950/22).

DATA AVAILABILITY

The data that support the findings of this article are not publicly available upon publication because it is not technically feasible, and/or the cost of preparing, depositing, and hosting the data would be prohibitive within the terms of this research project. The data are available from the authors upon reasonable request.

APPENDIX A: FORMULATION OF THE NONLINEAR VISCOUS MODEL

Throughout the paper, we compare the analytical approach with numerical simulations that account for both viscous dissipation of the fluid and higher nonlinearities in the elastic model. In this Appendix, we formulate this nonlinear model and elaborate on its numerical solution.

The flow of an unbounded fluid with density ρ_{f} and viscosity μ is described by three hydrodynamic fields: the two components of the fluid velocity vector, $\mathbf{v}(x, y, t) = (v_x(x, y, t), v_y(x, y, t))$, and the pressure $p(x, y, t)$. These fields evolve according to the conservation of mass and momentum, governed by the Navier-Stokes equations. Using the normalization described in the main text, these equations are given by

$$\nabla \cdot \mathbf{v} = 0, \tag{A1a}$$

$$\frac{D\mathbf{v}}{Dt} = \lambda \nabla \cdot \sigma, \tag{A1b}$$

where $D/Dt = \partial/\partial t + \mathbf{v} \cdot \nabla$ is the convective derivative, $\sigma_{ij} = -p\delta_{ij} + \frac{1}{\lambda R_e}(\frac{\partial v_i}{\partial x_j} + \frac{\partial v_j}{\partial x_i})$ is the fluid's stress tensor, and $R_e = (\rho_{\mathrm{f}}/\mu)\sqrt{B/\rho_{\mathrm{sh}} h}$ is the Reynolds number.

To model the interaction between the sheet and the fluid, we first need to define the position vector to a point on the sheet $\mathbf{x}_{\mathrm{sh}}(s, t) = (x_{\mathrm{sh}}(s, t), y_{\mathrm{sh}}(s, t))$ and the angle $\theta(s, t)$ between the tangent to the sheet and the x axis, where $s \in [0, 1]$ is the arclength parameter along the contour of the sheet. These three fields are not independent but satisfy the following geometric relations [20]:

$$\frac{\partial x_{\mathrm{sh}}}{\partial s} = \cos\theta, \tag{A2a}$$

$$\frac{\partial y_{\mathrm{sh}}}{\partial s} = \sin\theta. \tag{A2b}$$

At the sheet-fluid interfaces, no-slip conditions are implied:

$$\frac{\partial \mathbf{x}_{\mathrm{sh}}}{\partial t} = \mathbf{v}(x_{\mathrm{sh}}, y_{\mathrm{sh}}^{+}, t) \quad \text{and} \quad \frac{\partial \mathbf{x}_{\mathrm{sh}}}{\partial t} = \mathbf{v}(x_{\mathrm{sh}}, y_{\mathrm{sh}}^{-}, t), \tag{A3}$$

where y_{sh}^{+} (y_{sh}^{-}) correspond to the limit $y \to y_{\mathrm{sh}}$ from above (below). In addition, we need to satisfy the balance of moments and forces on the sheet. These equations are given by

$$\frac{\partial^2\theta}{\partial s^2} = -F_x \sin\theta + F_y \cos\theta, \tag{A4a}$$

$$\frac{\partial^2 \mathbf{x}_{\text{sh}}}{\partial t^2} = -\frac{\partial \mathbf{F}}{\partial s} + \left[\sigma(x_{\text{sh}}, y_{\text{sh}}^+, t) - \sigma(x_{\text{sh}}, y_{\text{sh}}^-, t)\right] \cdot \hat{\mathbf{n}}, \tag{A4b}$$

where $\sigma(x_{\text{sh}}, y_{\text{sh}}^+, t)$ $(\sigma(x_{\text{sh}}, y_{\text{sh}}^-, t))$ corresponds to the fluid's stress tensor when approaching the sheet from above (below), $\hat{\mathbf{n}} = (-\sin\theta, \cos\theta)$ is an upward normal unit vector, and $\mathbf{F}(s,t) = (F_x(s,t), F_y(s,t))$ is the vector of reaction forces in the sheet. Last, we prescribe the following hinged boundary conditions on the sheet's edges:

$$x_{\text{sh}}(0,t) = 0, \quad x_{\text{sh}}(1,t) = 1 - \Delta, \tag{A5a}$$

$$y_{\text{sh}}(0,t) = y_{\text{sh}}(1,t) = 0, \tag{A5b}$$

$$\frac{\partial \theta}{\partial s}(0,t) = \frac{\partial \theta}{\partial s}(1,t) = 0. \tag{A5c}$$

Equations (A1)–(A5), together with the condition that the velocity vanishes at infinity, complete the nonlinear formulation of the problem. In summary, given the sheet-to-fluid inertia ratio λ, the lateral displacement Δ, and the Reynolds number R_e, we can solve these equations for the hydrodynamic fields $\mathbf{v}(x,y,t)$ and $p(x,y,t)$ and the elastic fields $\{\mathbf{x}_{\text{sh}}(s,t), \theta(s,t), \mathbf{F}(s,t)\}$. We use the immersed boundary method to solve these equations numerically, as described, for example, in Ref. [9].

Reduction of the viscous equations to the inviscid model

The inviscid and irrotational model is obtained by setting the viscosity to zero, i.e., $\sigma_{ij} = -p\delta_{ij}$, and by introducing the velocity potential $\phi(x,y,t)$, such that $\mathbf{v} = \nabla\phi$. In this case, the continuity equation, Eq. (A1a), reduces to Laplace's equation, and the momentum equation [Eq. (A1b)] becomes integrable, yielding Bernoulli's equation [29]. These equations read

$$\nabla^2 \phi = 0, \tag{A6a}$$

$$\lambda p = -\frac{\partial \phi}{\partial t} - \frac{1}{2}|\nabla\phi|^2, \tag{A6b}$$

where the constant of integration in Eq. (A6b) can be absorbed in the potential function and is determined to keep the pressure zero at infinity. In addition, the no-slip boundary conditions at the sheet-fluid interfaces are replaced by no-penetration conditions that read

$$y = y_{\text{sh}}(x(s),t): \quad \frac{Dy_{\text{sh}}}{Dt} = \frac{\partial \phi}{\partial y}(x_{\text{sh}}, y_{\text{sh}}^+, t), \quad \text{and} \quad \frac{Dy_{\text{sh}}}{Dt} = \frac{\partial \phi}{\partial y}(x_{\text{sh}}, y_{\text{sh}}^-, t). \tag{A7}$$

The force balance equations on the sheet become

$$\frac{\partial^2 \theta}{\partial s^2} = -F_x \sin\theta + F_y \cos\theta, \tag{A8a}$$

$$\frac{\partial^2 \mathbf{x}_{\text{sh}}}{\partial t^2} = -\frac{\partial \mathbf{F}}{\partial s} + \left[p(x_{\text{sh}}, y_{\text{sh}}^-, t) - p(x_{\text{sh}}, y_{\text{sh}}^+, t)\right]\hat{\mathbf{n}}, \tag{A8b}$$

where we replace the fluid's stress tensor with the hydrodynamic pressure. The geometric constraints [Eq. (A2)] and the boundary conditions on the sheet [Eq. (A5)] remain unchanged compared with the viscous case.

This completes the reduction of the viscous model to the inviscid case. To summarize, given the sheet-to-fluid inertia ratio, λ, and the lateral displacement, Δ, Eqs. (A6)–(A8), and Eqs. (A2) and (A5) form a closed system of equations for determining the potential functions, and pressure $\phi(x,y,t)$ and $p(x,y,t)$, and the elastic fields $\{\mathbf{x}_{\text{sh}}(s,t), \theta(s,t), \mathbf{F}(s,t)\}$.

The inviscid formulation in the small-amplitude approximation

In this section, on top of the inviscid assumption, we also assume that the amplitude of the sheet relative to the flat configuration remains small, i.e., $\Delta \ll 1$. In this limit, the constraint of the lateral displacement [Eq. (A5a)] reduces to

$$\frac{1}{2}\int_0^1\left(\frac{\partial y_{\rm sh}}{\partial x}\right)^2 dx=\Delta. \tag{A9}$$

Similar expansion of the force balance equations [Eq. (A8)] to leading order in Δ yields

$$\frac{\partial^2 y_{\rm sh}}{\partial t^2}+\frac{\partial^4 y_{\rm sh}}{\partial x^4}+F_x(t)\frac{\partial^2 y_{\rm sh}}{\partial x^2}+p(x,0^+,t)-p(x,0^-,t)=0, \tag{A10}$$

where the pressure that the fluid exerts on the sheet is assumed to act at $y=0$ rather than at the exact height of the sheet, and the arclength parameter s is replaced by the Eulerian coordinate x, consistent with our level of approximation. The boundary conditions at the sheet's edges are

$$y_{\rm sh}(0,t)=y_{\rm sh}(1,t)=0, \tag{A11a}$$

$$\frac{\partial^2 y_{\rm sh}}{\partial x^2}(0,t)=\frac{\partial^2 y_{\rm sh}}{\partial x^2}(1,t)=0. \tag{A11b}$$

Furthermore, following Ref. [20], we approximate Bernoulli's equation [Eq. (A6b)] and the kinematic boundary conditions [Eq. (A7)] by

$$p(x,0^\pm,t)=-\frac{1}{\lambda}\left(\frac{\partial\phi}{\partial t}\right)_{y=0^\pm}, \tag{A12a}$$

$$\frac{\partial y_{\rm sh}}{\partial t}=\left(\frac{\partial\phi}{\partial y}\right)_{y=0^\pm}. \tag{A12b}$$

The continuity equation [Eq. (A6a)], which is already linear, remains unchanged in this reduced formulation.

Equations (A9)–(A12) and (A6a), in addition to the vanishing of the fluid's velocity at infinity, form closure and complete the formulation in the small-amplitude approximation. This formulation emanates from the minimization of Eq. (1), as is further discussed in the next section.

APPENDIX B: MINIMIZATION OF THE ACTION

In this Appendix, we show that minimization of the action $\mathcal{S}=\int_0^T\mathcal{L}dt$, where $\mathcal{L}$ is given by Eq. (1), yields the system's equations of motion in the small-amplitude approximation. To minimize the action, we add a small perturbation to the elastic and the hydrodynamic fields, i.e., $y_{\rm sh}\to y_{\rm sh}+\delta y_{\rm sh}$, $F_x\to F_x+\delta F_x$, and $\phi\to\phi+\delta\phi$, and expand to linear order in the perturbations. After some integrations by parts, this expansion reads

$$\begin{aligned}\delta\mathcal{S}=&\int_0^1\left[\frac{\partial y_{\rm sh}}{\partial t}\delta y_{\rm sh}+\frac{1}{\lambda}[\phi(x,0^-,t)-\phi(x,0^+,t)]\delta y_{\rm sh}\right]_0^T dx\\&-\int_0^T\left[\frac{\partial^2 y_{\rm sh}}{\partial x^2}\frac{\partial\delta y_{\rm sh}}{\partial x}-\left(\frac{\partial^3 y_{\rm sh}}{\partial x^3}+F_x(t)\frac{\partial y_{\rm sh}}{\partial x}\right)\delta y_{\rm sh}\right]_0^1 dt\\&-\int_0^T\int_0^1\left[\frac{\partial^2 y_{\rm sh}}{\partial t^2}+\frac{\partial^4 y_{\rm sh}}{\partial x^4}+F_x(t)\frac{\partial^2 y_{\rm sh}}{\partial x^2}+\frac{1}{\lambda}\left(\frac{\partial\phi}{\partial t}(x,0^-,t)-\frac{\partial\phi}{\partial t}(x,0^+,t)\right)\right]\delta y_{\rm sh}dxdt\\&+\int_0^T\int_0^1\left[\frac{1}{2}\left(\frac{\partial y_{\rm sh}}{\partial x}\right)^2-\Delta\right]\delta F_x dxdt+\frac{1}{\lambda}\int_0^T\int_0^1[\delta\phi(x,0^-,t)-\delta\phi(x,0^+,t)]\frac{\partial y_{\rm sh}}{\partial t}dxdt\\&-\frac{1}{\lambda}\int_0^T\oint_{C(t)}(\nabla\phi\cdot\hat{\mathbf{n}})\delta\phi ds+\frac{1}{\lambda}\int_0^T\int_{-\infty}^{\infty}\int_{-\infty}^{\infty}\nabla^2\phi\delta\phi dxdy,\end{aligned} \tag{B1}$$

where $C(t)$ is a closed contour around the sheet, ds is an infinitesimal line element along this contour, and $\hat{\mathbf{n}}$ is an outward unit normal vector to the enclosed region.

Given the initial conditions of the system and the hinged boundary conditions [Eq. (A11)], the first two lines vanish identically. The third line vanishes given that force balance in the y-direction is satisfied [Eqs. (A10) and (A12a)], and the first term in the fourth line equals zero given that the constraint over the end-to-end shortening is satisfied [Eq. (A9)].

In addition, the last term in the fifth line equals zero, given that the continuity equation [(A6a)] is satisfied in the fluid medium. Last, the second term in the penultimate line and the first term in the fifth line sum to zero when the kinematic boundary conditions are satisfied [Eq. (A12b)].

In summary, we showed that to linear order in the perturbations $\delta y_{\rm sh}$, δF_x, and $\delta\phi$, we have that $\delta\mathcal{S} = 0$. This completes the proof that the small-amplitude model emanates from the minimization of the action.

APPENDIX C: DERIVATION OF EQS. (5) AND (6)

In this Appendix, we elaborate on the procedure required to derive Eqs. (5) and (6) in the main text. Using Gauss theorem, we first replace the integral over the area of the domain [the last term in Eq. (1)] by a line integral. This gives

$$\begin{aligned}\mathcal{L} = &\int_0^1 \left[\frac{1}{2}\left(\frac{\partial y_{\rm sh}}{\partial t}\right)^2 - \frac{1}{2}\left(\frac{\partial^2 y_{\rm sh}}{\partial x^2}\right)^2 + F_x(t)\left(\frac{1}{2}\left(\frac{\partial y_{\rm sh}}{\partial x}\right)^2 - \Delta\right)\right.\\ &\left. + \frac{1}{\lambda}[\phi(x,0^-,t) - \phi(x,0^+,t)]\frac{\partial y_{\rm sh}}{\partial t}\right]dx + \frac{1}{2\lambda}\int_0^1 [\phi(x,0^+,t) - \phi(x,0^-,t)]\left(\frac{\partial \phi}{\partial y}\right)_{y=0} dx.\end{aligned} \tag{C1}$$

Then, we substitute the Fourier expansion of the height function and the potential function, Eqs. (2)–(4), in the Lagrangian, Eq. (C1), and integrate over the spatial coordinates. The result reads

$$\mathcal{L} = \frac{1}{4}\frac{dA_n}{dt}\frac{dA_k}{dt}\delta_{nk} - \frac{\pi^4 n^4}{4}A_n A_k \delta_{nk} + \frac{\pi^2 n^2}{4}F_x(t)A_n A_k\delta_{nk} - \frac{1}{2\pi\lambda n}a_k\frac{dA_n}{dt}\delta_{nk} + \frac{1}{\lambda}D_{nk}a_n a_k - F_x(t)\Delta, \tag{C2}$$

where D_{nk} is given in Eq. (6), and δ_{nk} is the Kronecker delta used here to emphasize that these terms are diagonal in the modal basis. Minimization of this Lagrangian with respect to $a_n(t)$ gives

$$a_n(t) = \frac{1}{2\pi k}\tilde{D}_{nk}^{-1}\frac{dA_k}{dt}. \tag{C3}$$

By substituting Eq. (C3) back into the Lagrangian, Eq. (C2), and collecting terms proportional to $\frac{dA_n}{dt}\frac{dA_k}{dt}$ and A_nA_k, we arrive to Eqs. (5) and (6) in the main text.

APPENDIX D: STABILITY AND MODERATE-TIME DYNAMICS OF THE THIRD MODE

In this Appendix, we deviate from the two-mode approximation adopted in the main text and analyze the stability and moderate-time evolution around the third mode of buckling. From a broader perspective, this analysis demonstrates that the formulation can be naturally extended beyond the two-mode approximation discussed in the main text. To this end, the Appendix is divided into two parts. First, we present the linear stability analysis around the third mode, and then, in the second part, discuss the subsequent relaxation of the sheet toward the first mode.

1. Linear stability around the third mode

In the third mode of buckling, the shape of the sheet comprises one and a half wavelengths. Within the small-amplitude approximation, this configuration is obtained by substituting $n = 3$

in Eq. (10), which yields $A_3 = 2\sqrt{\Delta}/(3\pi)$, $A_n = 0$ for all $n \neq 3$, and $F_x(0) = 9\pi^2$. To analyze the stability of this state, we substitute the above solution into the equations of order ϵ, Eq. (9), and determine from their solution the corresponding growth rate and eigenmode. To simplify the analysis, we retain only three modes of the sheet, since we expect that during relaxation, energy will be transferred predominantly into modes lower than the third, thereby reducing the bending deformation of the sheet.

From Eq. (9b), we immediately obtain that $\tilde{A}_3 = 0$. Therefore, while the static configuration is dominated by the third mode, it is primarily perturbed by the second and first modes. The solution of Eq. (9a) yields two real and positive growth rates. The larger of these is obtained from Eq. (9a) with $n = 2$, and corresponds to the case where $\tilde{A}_2$ remains arbitrary, while $\tilde{A}_1 = \tilde{F}_x = 0$. The growth rate is then given by

$$\text{second mode:} \quad \sigma = \frac{2\sqrt{5}\pi^2}{\sqrt{1 + \frac{|\tilde{D}_{22}^{-1}|}{8\pi^2\lambda}}}, \tag{D1}$$

where $|\tilde{D}_{22}^{-1}| \simeq 27.83$. We associate this growth rate with the second mode because its corresponding eigenfunction excites the second buckling mode.

The other positive growth rate is obtained from Eq. (9a) with $n = 1$ and $n = 3$. In that case, $\tilde{A}_1$ and $\tilde{F}_x$ differ from zero while $\tilde{A}_2 = 0$. The growth rate is given by

$$\text{first mode:} \quad \sigma = \frac{2\sqrt{2}\pi^2}{\sqrt{1 + \frac{c_1}{\pi^2\lambda}}}, \tag{D2}$$

where $c_1 = D_{11}(\tilde{D}_{11}^{-1})^2 + 2D_{13}\tilde{D}_{31}^{-1}\tilde{D}_{11}^{-1} + D_{33}(\tilde{D}_{31}^{-1})^2 - \tilde{D}_{11}^{-1} \simeq 8.23$. This growth rate is associated with the first mode because its corresponding eigenfunction excites the first buckling mode. In Figs. 6(a) and 6(b), we show that both predictions agree well with the numerical solution of the nonlinear and viscous equations.

Consequently, upon an arbitrary perturbation of the third-mode configuration, the first and second modes begin to grow exponentially. At early times, the second mode is expected to dominate the relaxation because it has the largest growth rate. However, the subsequent evolution may involve nonlinear interactions between the modes, and the sheet may oscillate between the second and third configurations before eventually relaxing toward the first mode. For completeness, we note that the scaling of both growth rates follows the same trends described in the main text: they converge to a constant in the limit of large λ and exhibit a square-root decay in the opposite limit.

An example of the dynamics at moderate times is shown in Fig. 6(c). In this figure, we use the numerical viscous formulation to integrate the governing equations in time, starting from arbitrary initial conditions, and then project the evolving configuration onto the first four modes. The temporal evolution of the corresponding modal amplitudes is shown in the figure. Initially, the configuration is dominated by the third mode, while all other modes are approximately zero. Since this configuration is unstable, the system escapes from the third mode. Because the growth rate associated with the second mode is the largest, the dynamics first relax toward the second mode, whereas relaxation toward the first mode occurs only at later times. Notably, the amplitude of the fourth mode remains small throughout the evolution, which indicates that there is no significant transfer of energy to higher modes.

The flow fields associated with each of these eigenmodes are shown in Figs. 6(d) and 6(e), and can be understood from their corresponding vortex distributions. The eigenfunction associated with the second mode, for which $\tilde{A}_2$ remains arbitrary, induces the vortex distribution $\gamma(x, t) \propto \cos(2\pi x)$ [see Eqs. (C3) and (4)], similar to that observed in Sec. III A when the sheet oscillates around the first mode. This distribution attains extremal values at the two edges, near $x = 0$ and $x = 1$, and at the midpoint, where the vorticity has the opposite sign to that at the edges. As a result, two vortices form near the edges, while a third, counter-rotating vortex appears near the midpoint of

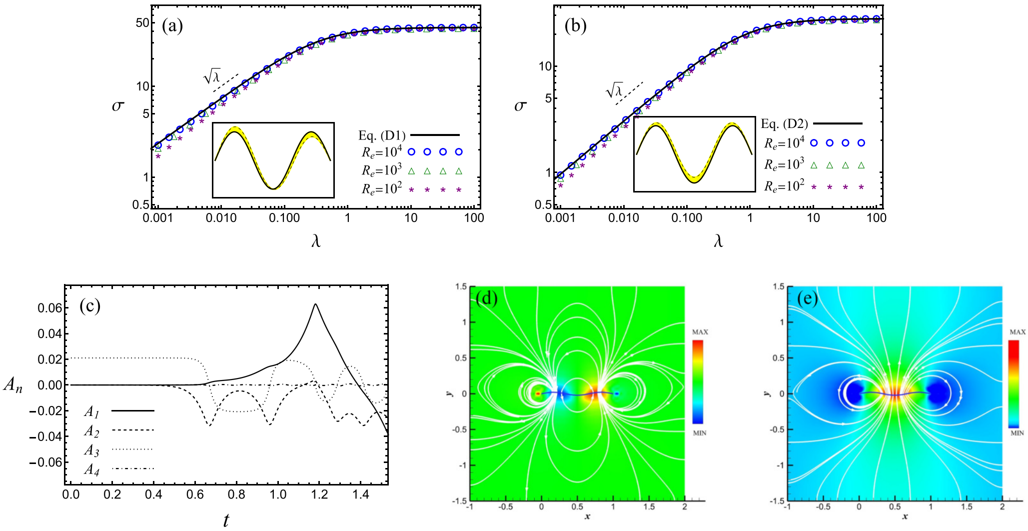

FIG. 6. Linear stability about the third mode of buckling. In panels (a) and (b), the growth rate σ is plotted as a function of λ. Solid lines correspond to the analytical predictions, while symbols represent the linear stability analysis of the viscous equations, with $\Delta = 0.01$. Inset: schematic illustration of the sheet's motion at early times. Panel (c) shows the temporal evolution of the modal amplitudes at later times, obtained from time integration of the viscous equations starting from arbitrary initial conditions. In panels (d) and (e), we show the numerically obtained flow-field eigenfunctions corresponding to the cases shown in panels (a) and (b), respectively, for $\lambda = 0.1$ and $R_e = 1000$.

the sheet. In contrast to the oscillations around the first mode, however, this flow field is expected to grow exponentially in time. Similarly, the eigenmode corresponding to the first buckling mode induces $\gamma(x,t) \propto \cos(\pi x)$. Consequently, the flow field resembles that shown in Fig. 3(c), where two counter-rotating vortices form near the edges of the sheet, accompanied by a net flow at the center; compare Figs. 6(c) and 3(c).

Keeping this picture of the excited modes in mind, we next turn to the analysis of the dynamics at moderate times, where nonlinear interactions between the dominant modes govern the subsequent relaxation of the sheet.

2. Dynamics at moderate times

Following the linear stability analysis of the third mode, we now turn to examine the subsequent evolution of the sheet at moderate times. Our goal here is not to develop a new theoretical framework, but rather to characterize the transition times associated with the relaxation of the sheet from the third mode to the second or first mode, and to compare numerical results with predictions obtained from low-order modal approximations.

To this end, we consider the following scenario: the sheet is initially prepared in the third buckling mode. Analytically, this configuration follows directly from Eq. (10). Obtaining the same configuration numerically, however, is more subtle. To do so, we divide the sheet into three equal segments along its arclength, namely, $s \in [0, 1/3]$, $s \in [1/3, 2/3]$, and $s \in [2/3, 1]$. In each segment, we solve the static equilibrium equations, (A2), (A4), and (A5), under the assumptions of zero inertia, $\partial^2 \mathbf{x}_{\rm sh}/\partial t^2 = 0$, and absence of external forcing, $\sigma = 0$. At the interfaces between adjacent segments, continuity of the sheet configuration and internal forces is imposed: the position $\mathbf{x}_{\rm sh}$, the angle θ, and the axial force F_x are all continuous. In addition, the vertical displacement satisfies $y_{\rm sh}(1/3) = y_{\rm sh}(2/3) = 0$. Solving this coupled boundary-value problem yields a static configuration corresponding to the third buckling mode.

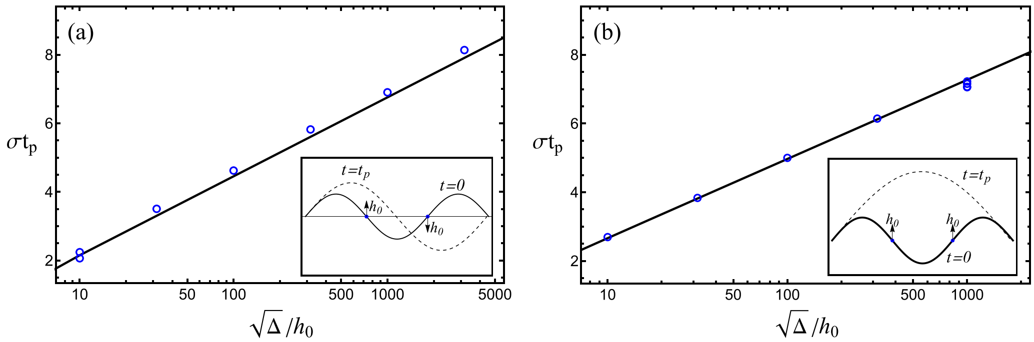

FIG. 7. The peak time multiplied by the growth rate, σt_p, as a function of $\sqrt{\Delta}/h_0$. In both panels, open blue circles represent results from numerical simulations with $R_e = 1000$, $\Delta = 0.1, 0.01$, $\lambda = 0.1, 0.01$, and $h_0 \in [10^{-5}, 10^{-2}]$. Solid lines correspond to the analytical predictions obtained from the two-mode approximation based on conservation of energy. (a) Asymmetric perturbation of the third buckling mode, which induces relaxation of the sheet toward the second buckling mode. The growth rate σ is given by Eq. (D1). (b) Symmetric perturbation of the third buckling mode, which induces relaxation toward the first buckling mode. The growth rate σ is given by Eq. (D2). In both panels, the insets schematically illustrate the imposed perturbation of the third mode and the corresponding mode toward which the sheet relaxes.

Here, however, we are not interested in an exact realization of the third mode, as this configuration represents a marginally stable state. Instead, our focus is on the dynamics resulting from a small, controlled perturbation of this mode. Rather than applying an arbitrary perturbation, we prescribe perturbations that selectively excite either the second or the first buckling mode. Specifically, an asymmetric perturbation is imposed by setting $y_{\text{sh}}(1/3) = -y_{\text{sh}}(2/3) = h_0$, which excites the second mode. Alternatively, a symmetric perturbation, $y_{\text{sh}}(1/3) = y_{\text{sh}}(2/3) = h_0$, selectively excites the first mode. In both cases, the perturbation amplitude satisfies $h_0 \ll 1$. These perturbations are demonstrated schematically in the insets of Fig. 7.

Following this initial setup, we integrate the viscous equations in time until the sheet reaches either the second or the first buckling mode, depending on the imposed perturbation. We then record the peak time t_p required for the system to reach this state. In the main text [see Eq. (14) and Fig. 5], we showed, using conservation of energy, that the modified peak time scales as $\sigma t_p \sim \ln(\sqrt{\Delta}/h_0)$. Here, we follow an analogous approach for both transition scenarios and use conservation of energy together with a two-mode approximation to recover the same scaling analytically. The two-mode approximation is implemented differently in the two cases. For the transition from the third to the second buckling mode, we set $A_1(t) = 0$ and retain only the modes $A_2(t)$ and $A_3(t)$. In contrast, for the transition from the third to the first buckling mode, we set $A_2(t) = 0$ and retain only $A_1(t)$ and $A_3(t)$. The comparison between these two cases and the numerical data is shown in Fig. 7, which demonstrates that the logarithmic scaling previously identified for the second-to-first mode transition persists for transitions involving higher buckling modes.

---

[1] H. Garg, P. G. Ledda, J. S. Pedersen, and M. Pezzulla, Passive viscous flow selection via fluid-induced buckling, Phys. Rev. Lett. **133**, 084001 (2024).

[2] R. Verzicco, Electro-fluid-mechanics of the heart, J. Fluid Mech. **941**, P1 (2022).

[3] M. Wehner, R. L. Truby, D. J. Fitzgerald, B. Mosadegh, G. M. Whitesides, J. A. Lewis, and R. J. Wood, An integrated design and fabrication strategy for entirely soft, autonomous robots, Nature (London) **536**, 451 (2016).

[4] J. B. Grotberg and O. E. Jensen, Biofluid mechanics in flexible tubes, Annu. Rev. Fluid Mech. **36**, 121 (2004).
[5] T. J. Pedley, B. S. Brook, and R. S. Seymour, Blood pressure and flow rate in the giraffe jugular vein, Philos. Trans. R. Soc. London, Ser. B **351**, 855 (1996).
[6] J. C. Mullarney and S. M. Henderson, Wave-forced motion of submerged single-stem vegetation, J. Geophys. Res.: Oceans **115**, 2010JC006448 (2010).
[7] G. Arena, R. M. J. Groh, A. Brinkmeyer, R. Theunissen, P. M. Weaver, and A. Pirrera, Adaptive compliant structures for flow regulation, Proc. R. Soc. A **473**, 20170334 (2017).
[8] D. P. Holmes, B. Tavakol, G. Froehlicher, and H. A. Stone, Control and manipulation of microfluidic flow via elastic deformations, Soft Matter **9**, 7049 (2013).
[9] K. Goncharuk, O. Oshri, and Y. Feldman, The immersed boundary method: A simple approach, J. Comput. Phys. **487**, 112148 (2023).
[10] O. Oshri, Vibrational modes of a thin sheet in a pressurized chamber, Phys. Rev. Fluids **10**, 013905 (2025).
[11] O. Oshri, K. Goncharuk, and Y. Feldman, Snap-induced flow in a closed channel, J. Fluid Mech. **986**, A12 (2024).
[12] Z. Li, Y. Wang, C. C. Foo, H. Godaba, J. Zhu, and C. H. Yap, The mechanism for large-volume fluid pumping via reversible snap-through of dielectric elastomer, J. Appl. Phys. **122**, 084503 (2017).
[13] J.-S. Park, J. Kim, A. Lee, and H.-Y. Kim, Snap-through inversion of elastic shells swelling via solvent diffusion, Soft Matter **19**, 8213 (2023).
[14] P. Rothemund, A. Ainla, L. Belding, D. J. Preston, S. Kurihara, Z. Suo, and G. M. Whitesides, A soft, bistable valve for autonomous control of soft actuators, Sci. Rob. **3**, eaar7986 (2018).
[15] M. Gomez, D. E. Moulton, and D. Vella, Passive control of viscous flow via elastic snap-through, Phys. Rev. Lett. **119**, 144502 (2017).
[16] E. Boyko, R. Eshel, K. Gommed, A. D. Gat, and M. Bercovici, Elastohydrodynamics of a pre-stretched finite elastic sheet lubricated by a thin viscous film with application to microfluidic soft actuators, J. Fluid Mech. **862**, 732 (2019).
[17] Y. Yang, Y. Wu, C. Li, X. Yang, and W. Chen, Flexible actuators for soft robotics, Adv. Intell. Syst. **2**, 1900077 (2020).
[18] J. H. Cartwright, O. Piro, and I. Tuval, Fluid dynamics in developmental biology: Moving fluids that shape ontogeny, HFSP J. **3**, 77 (2009).
[19] S. N. Ahsan and M. Aureli, Nonlinear oscillations of shape-morphing submerged structures: Control of hydrodynamic forces and power dissipation via active flexibility, J. Fluids Struct. **74**, 35 (2017).
[20] K. Goncharuk, Y. Feldman, and O. Oshri, Fluttering-induced flow in a closed chamber, J. Fluid Mech. **976**, A15 (2023).
[21] J. Katz, *Low-Speed Aerodynamics* (Cambridge University Press, Cambridge, 2001).
[22] L. D. Landau and E. M. Lifshitz, *Fluid Mechanics: Volume 6* (Elsevier, 1987).
[23] K. W. Mangler, Improper integrals in theoretical aerodynamics, Royal Aircraft Establishment, Report No. 2424 (1952).
[24] A. Pandey, D. E. Moulton, D. Vella, and D. P. Holmes, Dynamics of snapping beams and jumping poppers, Europhys. Lett. **105**, 24001 (2014).
[25] A. Draux, H.-A. B. Hua, P. Damman, and F. Brau, Relaxation dynamics of a flexible rod in a fluid, Phys. Rev. Fluids **6**, 114102 (2021).
[26] F. Box, D. O'Kiely, O. Kodio, M. Inizan, A. A. Castrejón-Pita, and D. Vella, Dynamics of wrinkling in ultrathin elastic sheets, Proc. Natl. Acad. Sci. USA **116**, 20875 (2019).
[27] L. Duchemin and N. Vandenberghe, Impact dynamics for a floating elastic membrane, J. Fluid Mech. **756**, 544 (2014).
[28] N. Vandenberghe and L. Duchemin, Impact on floating membranes, Phys. Rev. E **93**, 052801 (2016).
[29] H. Lamb, *Hydrodynamics* (Dover Publications, 1945).